Cleaner Energy Systems 3 (2022) 100044

Contents lists available at ScienceDirect

Cleaner Energy Systems

journal homepage: www.elsevier.com/locate/cles

A robust nonlinear backstepping control scheme for hybrid AC/DC microgrids to improve dynamic stability against external disturbances

Tushar Kanti Roy [a,*], Md Apel Mahmud [b]

[a] Department of Electronics & Telecommunication Engineering, RUET, Rajshahi 6204, Bangladesh
[b] Faculty of Engineering and Environment, Northumbria University Newcastle, Tyne and Wear, NE1 8ST, UK

ARTICLE INFO

Keywords:
Dynamic stability
Robust backstepping controller
Switching control signals
Hybrid AC/DC microgrid
Power balance

ABSTRACT

In this work, robust nonlinear controllers are designed for converters interfacing power generation and energy storage including DC- and AC-sides in hybrid AC/DC microgrid for improving the dynamic stability against external disturbances. The robust switching control inputs for all these interfacing converters and excitation as well as steam-valving control laws for the synchronous generators are determined using a nonlinear backstepping approach. The dynamic elements of the hybrid AC/DC microgrid are modeled by considering the effects of external disturbances where these disturbances reflect the effects of modeling errors, measurement noises, and parametric uncertainties. The robust control inputs for different elements in the microgrid are determined by guaranteeing the convergences of all relevant states, associated with different elements, toward their desired values while properly bounding the effects of disturbances. Control Lyapunov functions (CLFs) are formulated, during the proposed controller design process, to assess the dynamic stability. Simulation studies are conducted on a hybrid AC/DC microgrid to validate the effectiveness by observing the overall power balance with changes in the system while comparing with an existing sliding mode controller (ESMC). Simulation results clearly indicate robustness of the newly proposed controller through the improvement in the overall dynamic performance of the hybrid AC/DC microgrid over the ESMC.

1. Introduction

Microgrid offer several technical, environmental, and economic benefits as compared to traditional power grids (Hirsch et al., 2018; Parhizi et al., 2015). However, there several are challenges during the operation of microgrid which arise intermittencies of renewable energy sources (RESs) and variations in loads (Baghaee et al., 2018; Sun et al., 2015). The solar photovoltaic (PV) and wind generators are main RESs connected to microgrid for which the power generated by these generators relies on the solar irradiation and wind speed, respectively. The battery energy storage system (BESS) is another key component of microgrid that smoothes the fluctuations in RESs by storing excess energy into it and releasing energy based on the load condition. The solar PV unit and BESS mainly generate DC power which can be directly used to supply DC loads in many applications. This will also simplify the control structure as it does not require frequency and reactive power control (Katayama et al., 2019; Roy et al., 2018b). Similarly, the RESs which generate AC power can be used to supply AC loads and it eliminates the use of rectifiers for supplying DC loads (Mahmud et al., 2014a). Hence, the number of conversion stages can be reduced and at the same time, the control actions can be simplified by coupling both AC and DC microgrid using a bidirectional voltage source converter (VSC) for hybrid AC/DC microgrid (Loh et al., 2013b). However, the control of different elements remains an important point to focus as there are still challenges to deal with intermittencies in RESs and variations in loads within such hybrid microgrid. Therefore, it is worthwhile to design robust controllers for hybrid AC/DC microgrid which will ensure robustness against these factors.

There is a well-established literature to design and implement different linear and nonlinear controllers by separately considering DC and AC microgrids. A linear active stabilization technique is proposed in Radwan and Mohamed (2012) for DC microgrids by considering linearized models of different components and a linear state feedback control scheme is utilized in Pérez-Ibacache et al. (2018) for a similar purpose. The nonlinear backstepping (Roy and Mahmud, 2018) and feedback linearizing (Mahmud et al., 2017a) schemes are used for stabilizing DC microgrids over a range of operating scenarios. All these controllers primarily aim to ensure the dynamic stability of either DC or AC microgrid. A model-free proportional integral (PI) controller is presented in Liu et al. (2011), Ma et al. (2015) to regulate the output power of each component in a hybrid AC/DC microgrid where the power regulation is performed based on the coordination among different controllers. How-

* Corresponding author.
E-mail addresses: tkroy@ete.ruet.ac.bd (T.K. Roy), md.a.mahmud@northumbria.ac.uk (M.A. Mahmud).

https://doi.org/10.1016/j.cles.2022.100044
Received 10 January 2022; Received in revised form 18 October 2022; Accepted 16 November 2022
Available online 20 November 2022

ever, the PI controllers are not capable to ensure the dynamic stability during severe transients within the microgrid. A similar control is used in Sowmmiya and Govindarajan (2018) for a hybrid AC/DC microgrid where the controller is designed only for one component, a wound rotor induction generator, in order to control the voltage and frequency while there is no emphasis to control other components within the same microgrid. In Xia et al. (2017), a distributed controller is designed for the coordination among multiple parallel bidirectional VSCs in hybrid AC/DC microgrid. Though the controllers in Xia et al. (2017) ensure the desired power sharing, the dynamic voltage stability (i.e., for DC- and AC- bus) are not ensured.

The DC-bus voltage stability in a hybrid AC/DC microgrid is ensured in Loh et al. (2013a) by employing a generalized droop control scheme while guaranteeing the appropriate power sharing. However, the power sharing between two different microgrid (i.e., AC and DC) is not covered in Loh et al. (2013a). In Wang et al. (2018), the switching signal for the bidirectional VSC is regulated using a droop control scheme for exchanging power between AC and DC microgrid in a hybrid microgrid. The main problem of these droop controllers is their sensitivities to the errors in bus voltages (i.e., common DC- and AC-bus) at which the components of DC and AC microgrid are connected. Moreover, there are high chances of such errors as drrop coefficients for these droop controllers are determined based on linear characteristics of different elements in hybrid AC/DC microgrid. However, these characteristics are highly nonlinear and hence, maintaining the dynamic stability of the entire hybrid AC/DC microgrid would be difficult with droop controllers. On the other hand, the characteristics of different elements in hybrid AC/DC microgrids are highly nonlinear and hence, maintaining the dynamic stability of the entire hybrid AC/DC microgrids would be difficult with conventional droop controllers. An adaptive droop controller is presented in Gomez-Aleixandre et al. (2022), Sinha et al. (2021) to solve the drawbacks of conventional droop controllers that enhance voltage regulation by eliminating the impedance connected between the voltage controller and voltage source converter (VSC). Though an adaptive droop controller can provide satisfactory performance under heavy loading situations, however, its performance is similar to that of a conventional one under low and medium loading conditions. A similar adaptive droop controller based on a neuro-fuzzy inference system (NFIS) is proposed in Bevrani and Shokoohi (2013) to avoid the reliance on model configurations and line parameters. However, the computational burden on the entire hybrid AC/DC microgrid will be increased when the number of elements increases or the size of microgrids becomes larger.

The nonlinear characteristics of different elements in a hybrid AC/DC microgrid can be captured through nonlinear dynamical models. If the controllers for different elements are then designed based on these nonlinear models, the dynamic performance of hybrid AC/DC microgrid will be improved in a much better way and this can be evidenced from other applications in power systems (Mahmud et al., 2014c). Recently, an adaptive neural network (ANN) is used in Chettibi et al. (2018) to capture the nonlinearities of different elements in such a hybrid microgrid. However, its performance depends on the training set which is not required for the model-based control scheme. For islanded hybrid AC/DC microgrids, a new data-driven deep learning approach is proposed in Seyedi et al. (2022) where the control strategy predicts the rapid post-fault voltage instability rather than controlling the power sharing between the DC- and AC-sides. To alleviate this drawback, an effective power flow approach for hybrid AC/DC microgrids is proposed in Pullaguram et al. (2022). But the proper modeling of interlinking converters is absent in Pullaguram et al. (2022) though it is required to maintain the power balance and exact voltage relation between the DC- and AC-sides. However, the performance of these controllers depends on the training set which is not required for the model-based control scheme. To overcome this drawback, a model-based predictive controller is proposed in Rute-Luengo et al. (2022) for a hybrid AC/DC microgrid. However, the control actions in Rute-Luengo et al. (2022) are still obtained based on the droop control scheme. Moreover, improved performance may be obtained if precise information about the system parameters is available which is practically impossible. To avoid this limitation, another model-based nonlinear backstepping control approach is utilized in Roy et al. (2018a) for a hybrid microgrid in which controllers are designed for all elements to ensure the dynamic performance under different conditions. Though the controllers in Roy et al. (2018a) ensure the desired power balance, these are not robust against external disturbances which are very common during the real-time operation of microgrid. An adaptive backstepping controller combined with an active damper is proposed in Melath et al. (2022) to eliminate the aforementioned problems. However, the main focus in Melath et al. (2022) is only the control of the bidirectional VSCs to ensure the stability of the DC-bus voltage.

In hybrid AC/DC microgrid, external disturbances can be used to capture modeling errors, parametric uncertainties, and measurement noises. A nonlinear disturbance observer-based controller is presented in Wang et al. (2014) for hybrid microgrid where the observers estimate disturbances and the control actions regulate the DC-bus voltage according to its reference value. However, the control actions in Wang et al. (2014) are still based on the PI scheme which suffer from the robustness with changes in hybrid AC/DC microgrid as it is quite hard for the disturbance observers to accurately estimate all possible disturbances. Sliding mode controllers (SMCs) are very well-known for their inherent robustness against parameter variations as well as external disturbances and a nonlinear SMC is designed in Alam et al. (2016) in conjunction with a droop controller to control the grid voltage and current based on the dynamics of only the dynamics of the bidirectional VSC. However, the controllers are not designed for other sources including RESs and BESSs though the control of these components have significant impacts on the overall dynamic stability of hybrid AC/DC microgrid. By considering these facts, controllers for all elements in hybrid microgrid are presented in Baghaee et al. (2018) by using the sliding mode control scheme. However, SMCs are prone to unmodeled dynamics and there exist difficulties in selecting the sliding surface if the order of hybrid AC/DC microgrid becomes higher. The main problem associated with existing model-based nonlinear controllers for hybrid AC/DC microgrid can be summarized as:

- Designing controllers by considering the dynamical model of all components in hybrid AC/DC microgrids.
- Requiring to have an appropriate sliding surface for SMCs and well-known chattering effects that deteriorate the performance of the controller.
- The inability to provide robustness against external disturbances through the control actions of all components while eliminating the selection of the sliding surface.

The aforementioned problems can be solved using robust backstepping approach as it is capable to tackle external disturbances. This paper extends the idea in Roy et al. (2018a) by incorporating external disturbances with the model. The main priority of the proposed controller is to ensure that robustness against variations in renewable power generation due to intermittencies, changes in the load demand, and measurement noises. All these factors are considered external disturbances to formulate the problem for the proposed controller. Such changes can only be incorporated if the dynamical models of different components in the hybrid AC/DC microgrid are used to design the controller for which the corresponding dynamical models are also presented in this paper. The proposed robust backstepping scheme will ensure the overall stability of hybrid AC/DC microgrid as it derives all control inputs by ensuring the convergence of all states of different elements to their desired values. Any external disturbances can be incorporated within the dynamical models of these elements and lately, the control actions can be achieved by incorporating the effects of these disturbances. The dynamic stability is theoretically assessed by formulating control Lyapunov functions (CLFs) and simulation studies are presented for further justifying the effectiveness of the proposed robust controller over an ex-

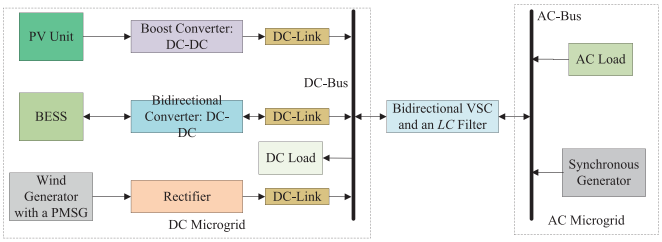

Fig. 1. Schematic diagram of the proposed hybrid AC/DC microgrid.

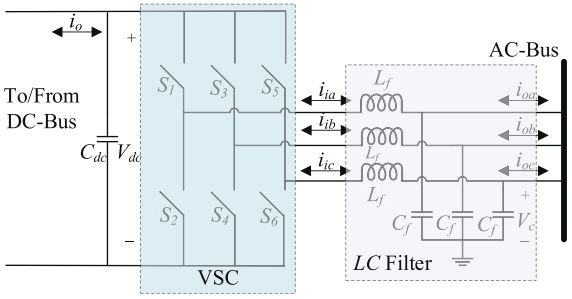

Fig. 2. Equivalent circuit diagram of a bidirectional VSC with an *LC* filter at the AC-side.

isting SMC (ESMC) as discussed in Alam et al. (2016). In summary, the key contributions of this work are:

- The detailed dynamical modeling of the solar PV unit, a PMSG-based wind turbine, a BESS, a synchronous generator along with it turbine-governor system and an output LC filter-based BVSC.
- Reducing the impact of variations in solar PV power and PMSG power on AC and DC loads is reduced using the BESS.
- The design of a new robust control scheme to manage power-sharing among variable generating sources (solar PV unit and PMSG-based wind generator) and loads including the BESS for minimizing DC-bus voltage variations during the system contingencies.
- A systematic way to analyze the stability and determine the control inputs for different components in microgrids.

2. Brief overview of the proposed hybrid AC/DC microgrid

Since the proposed robust controller will employed on different elements of a hybrid AC/DC microgrid, it is important to have an overview of this microgrid configuration. As presented in Fig. 1, there are two parts in the hybrid microgrid where the first part comprises all DC components which is actually a DC microgrid primarily supplying DC loads. The solar PV generation system, BESS, and a wind generation system having a permanent magnet synchronous generator (PMSG) are connected to the DC-bus. Similarly, the second part is an AC microgrid which has only AC components, mainly a lumped AC load along with a synchronous generator. A bidirectional VSC is used to link these DC and AC microgrid for exchange power from one side to other.

The microgrid transients due to the intermittencies in sunlight, wind speed, and load variations. The control actions of different elements need to be adjusted in order to tackle these transients and ensure the dynamic stability of hybrid AC/DC microgrid. For example, the DC-DC boost converter interfacing the solar PV unit with the DC-bus is controlled to regulate its output power while extracting the maximum power. Similarly, the switching control input for the rectifier regulates the wind power generation and the bidirectional converter coupling the BESS controls its charging and discharging. The switching control input for the bidirectional VSC needs to adjust based on the desired power exchange one side to another side. Finally, the excitation controller for the synchronous generator on the AC-side ensures the voltage stability while the steam-valve controller tackles load variations when the hybrid microgrid experiences external disturbances.

The modeling of different elements in Fig. 1 plays an important role to achieve the desired effectiveness of the control action. The dynamic stability of hybrid AC/DC microgrid can be ensured if dynamical models of different elements are used to derive control signals. Since the controller design with the proposed robust backstepping approach requires such dynamical models, the dynamical modeling of different elements in the microgrid in Fig. 1 is discussed in the following section.

3. Dynamical modeling of different elements hybrid microgrid

The proposed robust controller is designed based on the dynamical models of all elements within the microgrid structure in Fig. 1. Since the proposed control scheme is applied on all converters interfacing major components in the DC microgrid in the microgrid in Fig. 1 and the linking converter between AC- and DC-bus, the dynamical model of all these elements. It is worth to note that the AC-side of the bidirectional VSC includes an *LC* filter for minimizing the harmonic distortion and the effect of this filter is also included in the modeling. For the AC-side, both excitation and steam-valve control inputs are determined. All these dynamical models are briefly discussed in the subsections below.

3.1. Modeling of the bidirectional VSC having an LC filter on the AC-side

The equivalent circuit of a bidirectional VSC having an *LC* filter on the AC-side is shown in Fig. 2 and by incorporating the effects of external disturbances, the dynamical model of this converter can be obtained as (Nguyen et al., 2018):

$$\begin{aligned}
\dot{V}_{dc} &= \frac{i_o}{C_{dc}} - \frac{3}{2V_{dc}C_{dc}} V_{cd} I_{od} + d_{1VSC} \\
\dot{V}_{cd} &= \frac{1}{C_f} I_{id} + \omega V_{cq} - \frac{1}{C_f} I_{od} + d_{2VSC} \\
\dot{V}_{cq} &= \frac{1}{C_f} I_{iq} - \omega V_{cd} - \frac{1}{C_f} I_{oq} + d_{3VSC} \\
\dot{I}_{id} &= -\frac{1}{L_f} V_{cd} + \omega I_{iq} + \frac{1}{L_f} V_{dc} S_d + d_{4VSC} \\
\dot{I}_{iq} &= -\frac{1}{L_f} V_{cq} - \omega I_{id} + \frac{1}{L_f} V_{dc} S_q + d_{5VSC}
\end{aligned} \tag{1}$$

where V_{dc} denotes the voltage across the DC-link capacitor C_{dc}, i_o is the current flowing in or out at the DC-bus, V_{cd} is the direct-axis voltage across the filter capacitor (C_f), V_{cq} represents the quadrature-axis voltage across C_f, ω is the angular frequency, I_{id} is the direct-axis current at the input of the *LC* filter, I_{iq} is the quadrature-axis current at the input of the *LC* filter, I_{od} is the direct-axis current at the output of the *LC* filter, I_{oq} is the quadrature-axis current at the output of the *LC* filter, L_f is the filter inductance, S_d is the direct-axis switching signal of the VSC, and S_q is the quadrature-axis switching signal of the VSC. External disturbances are represented by d_{1VSC}, d_{2VSC}, d_{3VSC}, d_{4VSC}, and d_{5VSC} which are associated with the states of the VSC and the proposed robust backstepping approach will assist to derive switching control inputs, S_d and S_q.

3.2. Solar PV unit modeling with a DC-DC boost converter

Figure 3 shows an equivalent circuit diagram of a solar PV unit connected to the DC-bus through a DC-DC boost converter in which the PV cell is considered as a single diode model. By incorporating the effects of external disturbances, the dynamical model of the configuration in

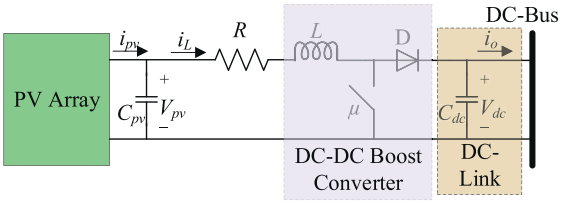

Fig. 3. Equivalent circuit diagram a solar power generation system coupled with a DC-DC boost converter.

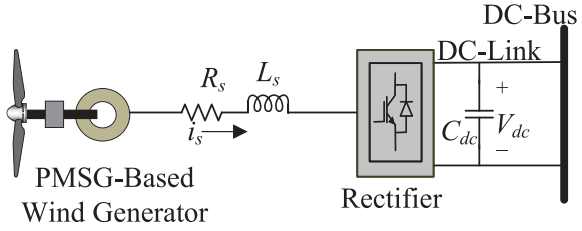

Fig. 4. Schematic diagram of a wind power generation system with the PMSG and a rectifier.

Fig. 3 can be expressed as (Mahmud et al., 2017b):

$$\begin{aligned}\frac{dV_{pv}}{dt} &= \frac{1}{C_{pv}}(i_{pv} - i_L) + d_{1PV}\\ \frac{di_L}{dt} &= \frac{1}{L}[-Ri_L + V_{pv} - (1-\mu)V_{dc}] + d_{2PV}\\ \frac{dV_{dc}}{dt} &= \frac{1}{C_{dc}}[(1-\mu)i_L - i_o] + d_{3PV}\end{aligned} \tag{2}$$

where V_{pv} represents the net output voltage of the PV unit with C_{pv} as the capacitance at the output of this unit which is used for filtering the voltage, R is the internal resistance of the inductor (L), i_L is the input current of the converter with μ as the switching control input and i_o denotes the current injection from the solar PV unit with V_{dc} as the voltage across the DC-link capacitor, C_{dc}. External disturbances are represented by d_{1PV}, d_{2PV}, and d_{3PV} are the external disturbances and μ obtained for this dynamical model.

3.3. PMSG-based wind generator modeling with a rectifier

The configuration of the wind generator with a rectifier is shown in Fig. 4 in which the rectifier is directly connected with the stator while the output of the rectifier is connected to the DC-bus. As the dynamic of the DC-link capacitor voltage can be tackled through all other states, it has not considered during the controller design in this paper. Based on Fig. 4, the dynamical model including external disturbances can be obtained as (Chinchilla et al., 2006; Mahmud et al., 2014b):

$$\begin{aligned}\dot{i}_{sd} &= -\frac{R_s}{L_S}i_{sd} + \omega_s i_{sq} + \frac{1}{L_s}V_{dc}m_{sd} + d_{1PMSG}\\ \dot{i}_{sq} &= -\frac{R_s}{L_S}i_{sq} - \omega_s i_{sd} - \frac{\omega_s \Psi}{L_s} + \frac{1}{L_s}V_{dc}m_{sq} + d_{2PMSG}\end{aligned} \tag{3}$$

where i_{sd} and i_{sq} represent direct- and quadrature-axis components of the stator current, respectively; R_s and L_s are the stator resistance and inductance, respectively; ω_s is the synchronously rotating angular frequency; Ψ is the stator flux; and m_{sd} and m_{sq} are direct- and quadrature-axis switching control signals for the rectifier, respectively. External disturbances are denoted by d_{1PMSG} and d_{2PMSG} to capture variations or modeling errors in the relevant equations. The proposed robust backstepping scheme is applied on this dynamical model to determine m_{sd} and m_{sq}.

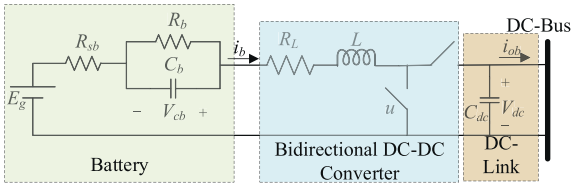

Fig. 5. Equivalent circuit represent of a battery coupling through a bidirectional DC-DC converter.

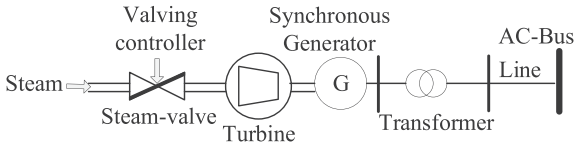

Fig. 6. Schematic diagram representing a synchronous generator connected to the AC-bus.

3.4. BESS modeling with a bidirectional DC-DC converter

Figure 5 shows the equivalent circuit of a BESS represented through an internal voltage source (E_g) with a series resistance (R_{sb}) including a parallel resistor (R_b)-capacitor (C_b) branch. This BESS is interfaced with a bidirectional DC-DC converter to the DC-link where the converter has an inductor (L) whose internal resistance isR_L while C_{dc} representing the capacitance of the DC-link with V_{dc} as the voltage across this capacitor. In Fig. 5, i_b is the current flowing through L. By applying circuit theories on Fig. 5, the dynamics of the BESS with a bidirectional DC-DC converter can be expressed as (Roy et al., 2016a):

$$\begin{aligned}\dot{V}_{cb} &= \frac{1}{C_{cb}}(i_b - \frac{V_{cb}}{R_b}) + d_{1BESS}\\ \dot{i}_b &= \frac{1}{L}[-(R_L + R_{sb})i_b + (1-u)V_{dc} - V_{cb} + E_g] + d_{2BESS}\\ \dot{V}_{dc} &= \frac{1}{C_{dc}}[(1-u)i_b - i_{0b}] + d_{3BESS}\end{aligned} \tag{4}$$

where V_{cb} denotes the voltage across C_b with u as the switching control input, and i_{ob} is the output current of the converter. External disturbances are expressed as d_{1BESS}, d_{2BESS}, and d_{2BESS} which capture the variations or modeling errors in the relevant equations. The dynamical model as represented by the set of Eq. (4) is used to derive u with the proposed control scheme.

3.5. Dynamical model of the synchronous generator

Figure 6 shows the connection of a synchronous generator to the AC-bus of the microgrid through a distribution line and transformer. As presented in Fig. 6, this generator is also coupled with the turbine-governor system. The excitation control action (V_c) maintains the terminal voltage (V_t) of the synchronous generator to its desired value while the steam-valve controller (P_c) adjusts the mechanical power input (P_m) with changes in load demands. Therefore, all relevant dynamics need to be included in modeling the controller for synchronous generator.

Recently, the two-axis model of synchronous generator is adopted for designing excitation controllers and the dynamical model of such a

generator can be expressed as (Roy et al., 2019):

$$\begin{aligned}
\dot{\delta} &= \omega - \omega_0 + d_{1SG} \\
\dot{\omega} &= -\frac{D}{2H}(\omega - \omega_0) + \frac{\omega_0}{2H}P_m - \frac{\omega_0}{2H}(E'_q I_q + E'_d I_d) + d_{2SG} \\
\dot{E}'_q &= -\frac{1}{T'_{do}}E'_q - \frac{(x_d - x'_d)}{T'_{do}}I_d + \frac{1}{T'_{do}}E_{fd} + d_{3SG} \\
\dot{E}'_d &= -\frac{1}{T'_{qo}}E'_d + \frac{(x_q - x'_q)}{T'_{qo}}I_q + d_{4SG} \\
\dot{E}_{fd} &= -\frac{E_{fd}}{T_A} + \frac{K_A}{T_A}(V_{ref} + V_c - V_t) + d_{5SG}
\end{aligned} \tag{5}$$

with δ as the rotor angle; ω as the rotor speed; ω_0 as the synchronous speed; D and H as damping and inertia constants, respectively; E'_q and E'_d as direct- and quadrature-axis transient voltages, respectively; I_d and I_q as direct- and quadrature-axis currents, respectively; T'_{do} and T'_{qo} as direct- and quadrature-axis transient open-circuit time constants, respectively; x'_d and x'_q as direct- and quadrature-axis transient reactances, respectively; x_d and x_q ass the direct- and quadrature-axis reactances, respectively; E_{fd} as the field excitation voltage, T_A as the time constant of the excitation system, K_A as the gain of the excitation system, and V_{ref} as the desired terminal voltage. External disturbances (e.g., parametric uncertainties or any type of faults or changes in loads) are represented by d_{1SG}, d_{2SG}, d_{3SG}, d_{4SG}, and d_{5SG}. The proposed excitation controller is designed by obtaining V_c for the dynamical model in (5).

Similarly, the dynamics of the turbine-governor system along with external disturbances can be written as (Roy et al., 2016b):

$$\begin{aligned}
\dot{P}_m &= -\frac{P_m}{T_T} + \frac{K_T}{T_T}X_E + d_{1TG} \\
\dot{X}_E &= -\frac{X_E}{T_G} + \frac{K_G}{T_G}P_C - \frac{K_G}{R_r\omega_0 T_G}\omega + d_{2TG}
\end{aligned} \tag{6}$$

where T_T and K_T are the time constant and gain of the turbine, respectively; X_E denotes the valve position with d_{1TG} as the external disturbances associated with the relevant equation; T_G and K_G are the time constant and gain of the governor, respectively; R_r is the regulation constant with d_{2TG} as the external disturbances associated with the relevant equation. The dynamical model in (6) is used to derive the control input, P_C by applying the robust backstepping approach.

3.6. Source, properties, and nature of disturbances different components

In hybrid AC/DC microgrids, the main sources of disturbances are weather conditions as the major power supply units are based on solar and ind power generation system. The changes in weather conditions will be reflected in the output power which in turn related to the voltage and currents. At the same time, the load demand in the system continuously changes. From Eqs. (1) to (5), it can be seen that all states are related to the voltage and current of different components in the system. This means the disturbance will change the relevant states of the system and these changes can be incorporated into the corresponding dynamical equations. Furthermore, the dynamical models of different components include the parameters of the system. It is difficult to obtain the exact values of these parameter and variations in parameters can be incorporated as disturbances as these appear in dynamical models. The implementation of controllers requires the measurement of different state variables, i.e., voltages and currents as appeared in different equations in this section. Noises inherently exist in measurement devices which need to be considered during the controller design process. The properties of all these noises or disturbances from different sources are random and these can be represented as the white Gaussian noise. The effects noises or disturbances from different sources can be lumped as one in the form of generalized disturbance corresponding to each dynamical equations as represented by Eqs. (1) to (6). Such disturbances can be modeled both stochastically and deterministically. In this work, a deterministic way is used by bounding the disturbance to a know value as discussed in the next section.

The detailed controller design process based on these models is outlined in the section below.

4. Robust backstepping controller design process

The proposed robust backstepping approach is used to determine switching control signals for all converters including control signals for excitation steam valve systems in the synchronous generator. Since the same approach is used for all dynamical models, the detailed and step-by-step design process is presented here for the bidirectional VSC converter with an *LC* filter at the AC-side while only derived control inputs are presented for all other components.

4.1. Robust backstepping controller design for the bidirectional VSC with an LC filter at the AC-side

The robust backstepping scheme is applied on the model in (1) to coordinate the power sharing between the AC- and DC-bus through the convergences of all state variables associated with this converter. Since the proposed scheme analyzes the convergences all associated state variables, there will be several steps to determine switching control inputs for the VSC.

Step 1: The controller design process can be started by analyzing the convergence of the error (e_{1VSC}) for tracking V_{dc}. If its desired value is $V_{dc(ref)}$, the tracking error will be as:

$$e_{1VSC} = V_{dc} - V_{dc(ref)} \tag{7}$$

For analyzing the convergence of e_{1VSC}, $\dot{e}_{1VSC}$ can be obtained as:

$$\dot{e}_{1VSC} = \frac{i_o}{C_{dc}} - \frac{3}{2V_{dc}C_{dc}}V_{cd}I_{od} + d_{1VSC} - \dot{V}_{dc(ref)} \tag{8}$$

There are different ways of assessing the dynamic stability or convergence and the energy function-based Lyapunov stability theory is the most commonly used one. Moreover, the selection of the stability analysis technique depends on the situation. For example, the traditional eigenvalue analysis is a common way if the system is linear. In this work, the stability is analyzed using the CLF in different steps as control objective in each step is to stabilize a state of the system. The state trajectory is represented through the energy, i.e., CLF of the associated state represented by the error. If the rate of change of energy is negative or zero (i.e., reduces with respect to the time), the system will be stable. In different steps, virtual control inputs are used until the original controller appears in the derivative of the CLF and this usually happens at the step. At that point, the control law can be obtained by satisfying condition, i.e., the rate of change of energy as negative or zero. Since this is a systematic way to determine the control input for the proposed scheme, the CLF is used in this work rather than any other stability analysis techniques. The CLF defining the energy associated with the state, for analyzing the convergence of e_{1VSC}, can be written as:

$$W_{1VSC} = \frac{1}{2}e^2_{1VSC} \tag{9}$$

It can be said that the error dynamic ($\dot{e}_{1VSC}$) will be stable if $\dot{W}_{1VSC}$ is negative definite ($\dot{W}_{1VSC} < 0$) or semi-definite ($\dot{W}_{1VSC} \leq 0$) for all e_{1VSC}. Thus, $\dot{W}_{1VSC}$ can be written and simplified as follows:

$$\dot{W}_{1VSC} = e_{1VSC}[\frac{i_o}{C_{dc}} - \frac{3V_{cd}I_{od}}{2V_{dc}C_{dc}} + d_{1VSC} - \dot{V}_{dc(ref)}] \tag{10}$$

At this point, the stabilizing function (α), corresponding to the next state variable (V_{cd}) which appears in Eq. (10), needs to be selected so that $V_{dc} = V_{dc(ref)}$, i.e., e_{1VSC} converges to zero and at the same time, $\dot{W}_{1VSC} < 0$ or $\dot{W}_{1VSC} \leq 0$. To do so, α can be chosen as:

$$\alpha = \frac{2V_{dc}C_{dc}}{3}[\frac{i_o}{C_{dc}}\dot{V}_{dc(ref)} - k_{1VSC}e_{1VSC}] \tag{11}$$

where k_{1VSC} is a positive design parameter assisting the convergence rate of e_{1VSC}. The stabilizing function (α) in Eq. (11) simplifies

Eq. (10) as follows:

$$\dot{W}_{1VSC} = -k_{1VSC}e_{1VSC}^2 + e_{1VSC}d_{1VSC} \tag{12}$$

If $e_{1VSC} = 0$, $\dot{W}_{1VSC} = 0$ and thus, indicating the stability of $\dot{e}_{1VSC}$. It is also essential to conduct the similar analysis for all remaining states while deriving the switching control inputs as discussed in the steps below.

Step 2: As α will ensure the zero tracking error (e_{2VSC}) for V_{cd}, this will be possible if $V_{cd} = \alpha$ for which the error can be defined as follows:

$$e_{2VSC} = V_{cd} - \alpha \tag{13}$$

and using second equation of (1), the dynamic of e_{2VSC} can be written as:

$$\dot{e}_{2VSC} = \frac{1}{C_f}I_{id} + \omega V_{cq} - \frac{1}{C_f}I_{od} - \dot{\alpha} \tag{14}$$

If $V_{cq(ref)}$ is the reference value of V_{cq}, the corresponding tracking error (e_{3VSC}) can be defined as follows:

$$e_{3VSC} = V_{cq} - V_{cq(ref)} \tag{15}$$

and its dynamic as:

$$\dot{e}_{3VSC} = \frac{1}{C_f}I_{iq} - \omega V_{cd} - \frac{1}{C_f}I_{oq} + d_{3VSC} - \dot{V}_{cq(ref)} \tag{16}$$

The stability of error dynamics in Eqs. (14) and (16) needs to be analyzed for which the CLF can be chosen as:

$$W_{2VSC} = W_{1VSC} + \frac{1}{2}e_{2VSC}^2 + \frac{1}{2}e_{3VSC}^2 \tag{17}$$

The derivative of W_{2VSC} can be simplified substituting the values of $\dot{W}_{1VSC}, \dot{e}_{2VSC}$, and $\dot{e}_{3VSC}$ from Eqs. (12), (14), and (16), respectively and written as follows:

$$\begin{aligned}\dot{W}_{2VSC} = {} & -k_{1VSC}e_{1VSC}^2 + e_{1VSC}d_{1VSC} + e_{2VSC}[\frac{1}{C_f}I_{id} \\ & +\omega V_{cq} - \frac{1}{C_f}I_{od} - \dot{\alpha}] + e_{3VSC}[\frac{1}{C_f}I_{iq} - \omega V_{cd} \\ & -\frac{1}{C_f}I_{oq} + d_{3VSC} - \dot{V}_{cq(ref)}] + e_{2VSC}d_{2VSC}\end{aligned} \tag{18}$$

The remaining two state variables I_{id} and I_{iq} appear in Eq. (18) and now, the stabilizing functions (α_d and α_q) for these states need to selected as follows:

$$\begin{aligned}I_{id} = \alpha_d &= -c_f(\omega V_{cq} - \tfrac{1}{C_f}I_{od} - \dot{\alpha} + k_{2VSC}e_{2VSC}) \\ I_{iq} = \alpha_q &= -c_f(k_{3VSC}e_{3VSC} - \omega V_{cd} - \tfrac{1}{C_f}I_{oq} - \dot{V}_{cq(ref)})\end{aligned} \tag{19}$$

with k_{2VSC} and k_{3VSC} as positive control parameters. The selections of stabilizing functions in Eq. (19) are mainly done in such a way that $\dot{W}_{2VSC} < 0$ or $\dot{W}_{2VSC} \leq 0$. In this situation, Eq. (18) can be simplified as:

$$\begin{aligned}\dot{W}_{2VSC} = {} & -k_{1VSC}e_{1VSC}^2 - k_{2VSC}e_{2VSC}^2 - k_{3VSC}e_{3VSC}^2 \\ & +e_{1VSC}d_{1VSC} + e_{2VSC}d_{2VSC} + e_{3VSC}d_{3VSC}\end{aligned} \tag{20}$$

If e_{1VSC}, e_{2VSC}, and e_{3VSC} converge to zero, $\dot{W}_{2VSC} = 0$ and thereby, indicating the negative semi-definiteness of $\dot{W}_{2VSC}$. As the stability of the error dynamics associated with I_{id} and I_{iq} is not analyzed and switching control inputs are still unknown, it is important to move towards the next steps.

Step 3: The stabilizing functions in Eq. (19) are generally virtual control inputs which do not guarantee the convergence of errors so far analyzed in previous steps. Since these functions (i.e., α_d and α_q) correspond to states I_{id} and I_{iq}, the corresponding error variables as defined below:

$$\begin{aligned}e_{4VSC} &= I_{id} - \alpha_d \\ e_{5VSC} &= I_{iq} - \alpha_q\end{aligned} \tag{21}$$

whose dynamics can be simplified as:

$$\begin{aligned}\dot{e}_{4VSC} &= -\frac{1}{L_f}V_{cd} + \omega I_{iq} + \frac{1}{L_f}V_{dc}S_d + d_{4VSC} - \dot{\alpha}_d \\ \dot{e}_{5VSC} &= -\frac{1}{L_f}V_{cq} - \omega I_{id} + \frac{1}{L_f}V_{dc}S_q + d_{5VSC} - \dot{\alpha}_q\end{aligned} \tag{22}$$

Equation (22) includes switching control signals for the VSC, i.e., S_d and S_q which should be selected in such a way that all errors, i.e., e_{1VSC} to e_{5VSC} become zero. For analyzing convergences of all errors associated with the bidirectional VSC, the CLF needs to be selected as follows:

$$W_{3VSC} = W_{2VSC} + \tfrac{1}{2}e_{4VSC}^2 + \tfrac{1}{2}e_{5VSC}^2 \tag{23}$$

whose derivative can be simplified as:

$$\begin{aligned}\dot{W}_{2VSC} = {} & -k_{1VSC}e_{1VSC}^2 - k_{2VSC}e_{2VSC}^2 - k_{3VSC}e_{3VSC}^2 \\ & +e_{1VSC}d_{1VSC} + e_{2VSC}d_{2VSC} + e_{3VSC}d_{3VSC} \\ & +e_{4VSC}[-\frac{1}{L_f}V_{cd} + \omega I_{iq} + \frac{1}{L_f}V_{dc}S_d + d_{4VSC} - \dot{\alpha}_d] \\ & +e_{5VSC}[-\frac{1}{L_f}V_{cq} - \omega I_{id} + \frac{1}{L_f}V_{dc}S_q + d_{5VSC} - \dot{\alpha}_q]\end{aligned} \tag{24}$$

For the stability of the entire converter, $\dot{W}_{2VSC}$ in Eq. (24) needs to be either $\dot{W}_{2VSC} < 0$ or $\dot{W}_{2VSC} \leq 0$ which will be possible if S_d and S_q are selected as follows:

$$\begin{aligned}S_d = {} & \frac{L_f}{V_{dc}}[\frac{1}{L_f}V_{cd} - \omega I_{iq} + \dot{\alpha}_d - k_{4VSC}e_{4VSC} - F_{4VSC} \\ & sgn(e_{4VSC})] - e_{1VSC}F_{1VSC}sgn(e_{1VSC}) - e_{2VSC} \\ & F_{2VSC}sgn(e_{2VSC})\end{aligned} \tag{25}$$

$$\begin{aligned}S_q = {} & \frac{L_f}{V_{dc}}[\frac{1}{L_f}V_{cq} + \omega I_{id} + \dot{\alpha}_q - k_{5VSC}e_{5VSC} - F_{5VSC} \\ & sgn(e_{5VSC})] - e_{3VSC}F_{3VSC}sgn(e_{3VSC})\end{aligned}$$

where k_{4VSC} and k_{5VSC} are positive control parameters with sgn as the *signum* function defined by the following equation:

$$sgn(e) = \begin{cases}+1 & \text{if } e > 0 \\ 0 & \text{if } e = 0 \\ -1 & \text{if } e < 0\end{cases} \tag{26}$$

With the switching control inputs in (25), Eq. (24) can be simplified as:

$$\begin{aligned}\dot{W}_{2VSC} = {} & -k_{1VSC}e_{1VSC}^2 - k_{2VSC}e_{2VSC}^2 - k_{3VSC}e_{3VSC}^2 \\ & -k_{4VSC}e_{4VSC}^2 - k_{5VSC}e_{5VSC}^2 + e_{1VSC}(d_{1VSC} - \\ & F_{1VSC}sgn(e_{1VSC}) + e_{2VSC}(d_{2VSC} - F_{2VSC}sgn \\ & (e_{2VSC}) + e_{3VSC}(d_{3VSC} - F_{3VSC}sgn(e_{3VSC}) + \\ & e_{4VSC}(d_{4VSC} - F_{4VSC}sgn(e_{4VSC}) + e_{5VSC}(d_{5VSC} \\ & -F_{5VSC}sgn(e_{5VSC})\end{aligned} \tag{27}$$

which will be be either $\dot{W}_{2VSC} < 0$ or $\dot{W}_{2VSC} \leq 0$ if the following conditions are satisfied:

$|\, d_{1VSC} \,| \leq F_{1VSC}$, $|\, d_{2VSC} \,| \leq F_{2VSC}$, $|\, d_{3VSC} \,| \leq F_{3VSC}$, $|\, d_{4VSC} \,| \leq F_{4VSC}$, and $|\, d_{5VSC} \,| \leq F_{5VSC}$ with F_{1VSC}, F_{2VSC}, F_{3VSC}, F_{4VSC}, and F_{5VSC} as known bounds. Therefore, it can be summarized that the robust backstepping scheme can be employed to determine the switching control signals which stabilize the bidirectional VSC with an LC filter at the AC-side. The same procedure is applied to determine the switching control inputs for all remaining converters including the excitation and steam valve controllers. However, these design procedures have not been repeated in this paper rather than just mentioning the derived control inputs in the following subsections.

4.2. Robust backstepping switching control signal for the converter coupling the solar PV unit

The dynamical model in (2) is utilized to derive the switching control input for the converter coupling the solar PV unit. By applying the proposed scheme, this switching control input is derived as the derivative that can be written as follows:

$$\begin{aligned}\dot{\mu} = \frac{1}{V_{dc}}[\frac{R}{L}\frac{di_L}{dt} + \mu_1\dot{V}_{dc} + \dot{\gamma} - \dot{V}_{pv} - k_{2PV}\dot{e}_{2PV} - k_{3PV} \\ e_{3PV} - e_{3PV}F_{3PV}sgn(e_{3PV})] - e_{2PV}F_{2PV}sgn(e_{2PV}) \\ -e_{1PV}F_{1PV}sgn(e_{1PV})\end{aligned} \tag{28}$$

where e_{1PV}, e_{2PV}, and e_{3PV} are error variables; $\mu_1 = 1 - \mu$, $\gamma = C_{pv}[\dot{V}_{pv(ref)} - k_4 e_4]$ with k_{1PV}, k_{2PV}, and k_{3PV} are positive control parameters. The signum function in Eq. (28) is similar to that as in Eq. (26) while F_{1PV}, F_{2PV}, and F_{3PV} are bounds to external disturbances with $|\, d_{1PV} \,| \leq F_{1PV}$, $|\, d_{2PV} \,| \leq F_{2PV}$, and $|\, d_{3PV} \,| \leq F_{3PV}$. An integral action is used during the implementation of this control input.

4.3. Robust backstepping switching control signals for the rectifier coupling a wind generator

The dynamical model in (3) is utilized to derive the switching control inputs for the rectifier coupling the wind generator. By applying the proposed scheme, switching control inputs for the rectifier are derived as follows::

$$\begin{aligned}m_{sd} = \frac{R_s}{L_s}i_{sd} + \frac{L_s}{V_{dc}}[\dot{i}_{sd(ref)} - \omega_s i_{sq} - k_{1PMSG}e_{1PMSG} \\ -e_{1PMSG}F_{1PMSG}sgn(e_{1PMSG})] \\ m_{sq} = \frac{R_s}{L_s}i_{sq} + \frac{L_s}{V_{dc}}[\dot{i}_{sq(ref)} + \omega_s i_{sd} + \frac{\omega_s}{L_s}\hat{\Psi} \\ -k_{2PMSG}e_{2PMSG} - e_{2PMSG}F_{2PMSG}sgn(e_{2PMSG})]\end{aligned} \tag{29}$$

where e_{1PMSG} and e_{2PMSG} are error variables with k_{1PMSG} and k_{2PMSG} as positive control parameters while F_{1PMSG} and F_{2PMSG} are known bounds to external disturbances with $|\, d_{1PMSG} \,| \leq F_{1PMSG}$ and $|\, d_{2PMSG} \,| \leq F_{2PMSG}$.

4.4. Robust backstepping control signal for the bidirectional DC-DC converter coupling the BESS

The dynamical model in (4) is utilized to derive the switching control inputs for the converter coupling with the BESS. By applying the proposed scheme, this switching control input is derived as the derivative that can be written as follows:

$$\begin{aligned}\dot{u} = \frac{L}{V_{dc}}(A + k_{3BESS}e_{3BESS}) - e_{1BESS}F_{1BESS}sgn \\ (e_{1BESS}) - e_{2BESS}F_{2BESS}sgn(e_{2BESS}) - e_{3BESS} \\ F_{3BESS}sgn(e_{3BESS})\end{aligned} \tag{30}$$

where

$$A = \frac{1}{L}[-(R_L + R_{sb})\frac{di_b}{dt} - \dot{V}_{cb} + E_g] - \ddot{\alpha}_b + k_{2BESS}\dot{e}_{2BESS}$$

$$+\Delta[\frac{1}{C_{dc}}(i_b - i_{ob})] \text{ and } \Delta = \frac{1-u}{L}d_{3BESS}$$

with e_{1BESS}, e_{2BESS}, and e_{3BESS} are error variables and k_{1BESS}, k_{2BESS}, and k_{3BESS} as positive control parameters while F_{1BESS}, F_{2BESS}, and F_{3BESS} are known bounds to external disturbances with $|\, d_{1BESS} \,| \leq F_{1BESS}$, $|\, d_{2BESS} \,| \leq F_{2BESS}$, and $|\, d_{3BESS} \,| \leq F_{3BESS}$. An integral action is used during the implementation of this control input.

4.5. Robust backstepping excitation and steam-valve control inputs for the synchronous generator

The dynamical model in (5) is utilized to derive the excitation control input for the synchronous generator. By applying the proposed scheme, the excitation control input is derived as follows:

$$\begin{aligned}V_c = \frac{E_{fd}}{K_A} - (V_{ref} - V_t) + \frac{T_A}{K_A}\dot{\beta}_3 - \frac{T_A}{K_A}k_{5SG}e_{5SG} \\ -\frac{T_A}{K_A}e_{5SG}F_{5SG}sgn(e_{5SG}) - e_{4SG}F_{4SG}sgn(e_{4SG}) \\ -e_{3SG}F_{3SG}sgn(e_{3SG}) - e_{2SG}F_{2SG}sgn(e_{2SG}) - \\ e_{1SG}F_{1SG}sgn(e_{1SG})\end{aligned} \tag{31}$$

where e_{1SG}, e_{2SG}, and e_{5SG} are error variables with $k_{1SG}, k_{2SG}, k_{3SG}, k_{4SG}$, and k_{5SG} as positive control parameters while $|\, d_{1SG} \,| \leq F_{1SG}$, $|\, d_{2SG} \,| \leq F_{2SG}$, $|\, d_{3SG} \,| \leq F_{3SG}$, $|\, d_{4SG} \,| \leq F_{4SG}$, and $|\, d_{5SG} \,| \leq F_{5SG}$ are known bounds to external disturbances for the synchronous generator.

Similarly, the dynamical model in (6) is utilized to derive the steam-valve control input for the synchronous generator.By applying the proposed scheme, the excitation control input is derived as follows:

$$\begin{aligned}P_C = -\frac{T_G}{K_G}(-\frac{X_E}{T_G} - \frac{K_G\omega}{R_r\omega_0 T_G} - \dot{\beta}_4 + k_{2TG}e_{2TG} \\ +F_{2TG}sgn(e_{2TG})) - e_{1TG}F_{1TG}sgn(e_{1TG})\end{aligned} \tag{32}$$

with

$$\beta_1 = \frac{P_m}{I_q} - \frac{D}{I_q\omega_0}(\omega - \omega_0) + \frac{2H}{I_q\omega_0}(\omega - \omega_0)k_{1SG} + \frac{2H}{I_q\omega_0}\dot{\beta},$$

$$\beta_2 = \frac{2H}{I_q\omega_0}k_{2SG}e_{2SG},\ \beta = -k_{1SG}e_{1SG}$$

$$\beta_3 = E'_q + (x_d - x'_d)I_d + T'_{do}\beta_1 - T'_{do}k_{3SG}e_{3SG}, \text{ and}$$

$$\beta_4 = \frac{T_T}{K_T}(\frac{P_m}{T_T} - k_{1TG}e_{1TG})$$

where e_{1TG} and e_{2TG} are error variables with k_{1TG} and k_{2TG} as positive control parameters while $|\, d_{1TG} \,| \leq F_{1TG}$ and $|\, d_{2TG} \,| \leq F_{2TG}$ are known bounds to external disturbances for the turbine-governor system.

The designed control inputs for different elements are used to analyze the performance of the hybrid AC/DC microgrid under varying operating conditions.

5. Performance analysis of designed controllers

The derived control inputs for different elements of the microgrid in Fig. 1 are used for analyzing the dynamic performance. The Simscape tool in MATLAB/Simulink platform is used to develop the microgrid in Fig. 1. The voltage at the DC-bus of this microgrid is considered as 640 V while the maximum power rating of the solar unit as 12 kW during the standard atmospheric condition at which the solar irradiation and environmental temperature are considered as 1 kW/m^2 and 25°C, respectively. The rated output power of the wind generation system is considered 25 kW. The capacity of the battery (a Lithium-ion battery is used for the simulation) is considered as 150 Ah while its nominal voltage is 300 V. The maximum value of the DC load is considered as 15 kW while it is 30 kW at the AC-bus. The generalized representation of the implementation block diagram of all controllers is shown in Fig. 7 which clearly depicts that all these controllers use the physical properties such as voltage, current, etc. as feedback from the system where the system model includes external disturbances in the form of parameter variations, measurement noises, and modeling errors. It is worth to note that the bounds on external disturbances for different elements are calculated based on slight variations in parameters from their nominal values along with modeling errors and the effects of measurement noises are captured in the form of white Gasussian noises. These

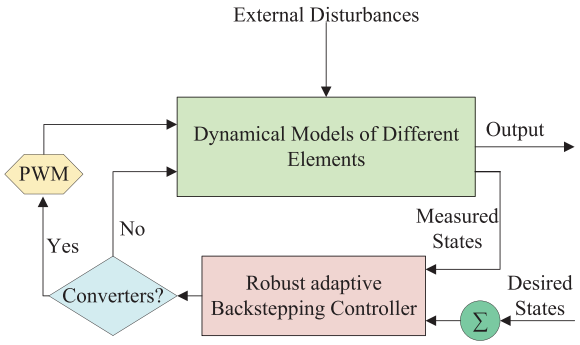

Fig. 7. Implementation block diagram.

physical properties along with the bounds on external disturbances and nominal parameters of the respective components are used to formulate the control signal which in turn ensures the desired dynamic performance of the system. The control inputs obtained for different components in Section 4 includes the bounded disturbance (F). Therefore, the proposed control scheme of different components in hybrid AC/DC microgrid is capable to ensure the robustness against disturbances. Since the nature of disturbances in different components are modeled as the White Gaussian noises which are added with all measured signals during the implementation of the proposed controller, the proposed scheme ensures the robustness gainst such disturbances. Finally, pulse width modulation (PWM) schemes are utilized for converters while these control inputs are directly implemented for the excitation and steam-valve systems of the synchronous generator. The control signals are derived in the MATLAB/Simulink for all elements of the microgrid in Fig. 1. During the simulation, the switching and sampling frequencies are considered as 5 kHz and 10 kHz, respectively. It is well-known that one of the key goals for designing and implementing new controllers is to achieve a faster response during the transient. For the proposed scheme, the larger values of these user-defined parameters will ensure fast transient performance. However, such large values of user-defined parameters or gains are not always useful as these degrade the performance of the controller by amplifying the overshoot and providing undesirable disturbance rejection. As a result, it is crucial to trade-off among different performance parameters when optimizing these gains. The necessary tracking criteria (such as no offsets, minimal overshoots, fast settling time, etc.), proper level of disturbance rejection, and resilience against parametric restrictions are required components of these performance characteristics. Therefore, all user-defined parameters are carefully selected to ensure adequate tracking performance because the focus of this work is on disturbance rejection and resistance against uncertainty. In this work, gain parameters are tuned by considering all these facts while carrying out the time-domain simulation.

The robustness of the controller is assessed through the performance evaluation under a range of scenarios and checked whether the power balance is achieved or not. In this section, simulations are conducted with changes in solar and wind power generation due to changes in atmospheric conditions along with changes in load demands. All these changes are reflected as external disturbances through defined bounds in the control signals of different components. In this simulation, it is considered that DC part of the microgrid operates first for which the DC-bus voltage is built by activating the solar PV unit at the beginning. The wind generator then comes into the operation and subsequently, the BESS and the DC load. The synchronous generator and AC loads start once the DC part is fully operating. The performance of the newly designed nonlinear robust backstepping controller (NRBC) is compared with an ESMC as presented in Alam et al. (2016) by considering a range of operating scenarios. The performance of the controller is evaluated by following systematic way to reflect the changes in operating conditions with steps as indicated below:

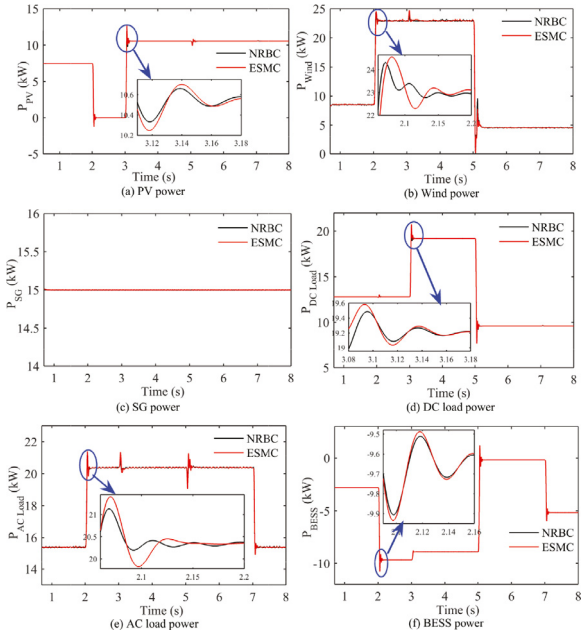

Fig. 8. Power profiles of all elements in the microgrid under different operating scenarios.

- **Step 1:** Start with the partial solar irradiation (, i.e., 780 W/m^2) rather than the standard irradiation (i.e., 1000 W/m^2), turn on the wind generator at a nominal wind speed, keep the synchronous in operation, maintain the load in a way that there will be power exchange between DC- and AC-sides.
- **Step 2:** Turn off the solar generator, increase the wind speed from the nominal speed in the previous step, increase the load on the AC side and keep the power generator by the synchronous generator and DC load similar to that of the previous step.
- **Step 3:** Turn on the solar generator to operate under the standard irradiation, reduce the wind speed to a value lower than the nominal value as in the first step, and reduce the DC load while keeping everything else is similar to that in the previous step.

As indicated earlier, the disturbances are added to all measured signals and kept throughout the simulation.

Initially, it is assumed that the solar system does not operate under the standard atmospheric condition as the solar irradiation is set as 780 W/m^2 which corresponds the solar power generation as 7.467 kW. At this point, the PMSG-based wind farm is delivering 8.547 kW when it is operating with the wind speed of 9 m/s. This operation continues until $t = 2$ s when the power consumptions by DC and AC loads are 12.8 kW and 15.42 kW, respectively. For this condition, the total power generation at the DC-side is 16.014 kW while having the total load demand on this side as 12.8 kW and hence, there will still be 3.214 kW extra DC power. This extra power from the DC-side can be either stored or transferred into the AC-side depending on the state-of-charge (SOC) of the battery and loads in AC-side. The load demand on the AC-side will not be fulfilled from the power generated by the synchronous generator as it generates 15 kW and consumptions on this side is 15.42 kW. Thus, it is essential to import 0.42 kW power from the DC- to AC-side which can easily be done by regulating the switching actions of the bidirectional VSC. As the battery still have the ability to store energy, it will store the energy for the remaining leftover power, i.e., 2.794 kW. All these are clearly presented through the power profiles (until $t = 2$ s) of different elements as demonstrated in Fig. 8. The DC-link voltage in this situation can be observed in Fig. 9 which is maintained at its desired values through the designed control actions of different components. Since there are no transients in the system until $t = 2$ s, it is hard to dis-

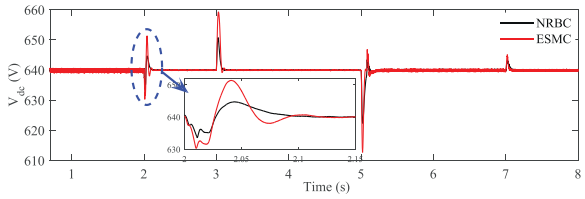

Fig. 9. The voltage of the DC-bus under different operating scenarios.

tinguish the performance of the designed NRBC and ESMC. However, the changes in performances can be distinguished during transient conditions as discussed in the remaining parts of this section.

During the next step of the simulation, the microgrid experiences some transients at $t = 2$ s due to the changes in the power generation (e.g., varying solar irradiation and wind speed) and the AC load. The following changes occur at $t = 2$ s:

- The solar unit does not generate power, i.e., the generation decreases from 7.467 kW to 0 kW as depicted in Fig. 8(a),
- The wind speed increases from 9 m/s to 13 m/s which in turn increases the wind power generation from 8.547 kW to 23 kW as shown in Fig. 8(b), and
- The AC load increases from its previous value (i.e., 15.42 kW) to 20.4 kW as shown in Fig. 8(e).

However, all other conditions remain the same, i.e., the DC load is still 12.8 kW and the synchronous generator is supplying 15 kW. This operation continues until $t = 3$ s and during this period, the DC-side is still generating more power than the load demand while the AC-side still has a power shortage. However, the power balance can be achieved by exporting the generated power from the DC- to AC-side. In such a situation, more energy will be stored into the BESS as the overall power excess is higher than the previous step which can be found in Fig. 8(f). From Figs. 8 and 9 demonstrate that the power profiles of different components (except for the synchronous generator) and the DC-link voltage experience transients at $t = 3$ s due to changes in the microgrid and the designed NRBC tackles these transient in better way (in terms of both overshoot and settling time) as compared to the ESMC.

The hybrid AC/DC microgrid experiences another transient at $t = 3$ s when the following changes occur:

- The power generation from the solar system increases from 0 kW to 10.55 kW as shown in Fig. 8(a) due to changes in the irradiation from its previous value (0 kW/m^2) to 1 kW/m^2 and
- The DC load rises further from 12.8 kW to 19.2 kW as shown in Fig. 8(d).

The power profiles of all remaining components remain as the same to that of the previous operating interval, i.e., from $t = 2$ s to $t = 3$ s. In this scenario, the bidirectional VSC will export the similar power from the DC- to AC-side as discussed in the previous step. However, the energy stored by the battery will reduce from 10 kW to 8.9 kW as the increment in the DC load consumes extra power which is presented in the power profile of the BESS in Fig. 8(f). This operating condition sustains until $t = 5$ s. However, the power profile of the synchronous generator is not disturbed though this is not the case for other components. The main reason behind this is the high inertia of the synchronous generator. The severity of this transient is bit higher than the previous case and clearly reflected in the DC-bus voltage in Fig. 9.

The power profiles of the microgrid is further disturbed at $t = 5$ s due to the following transients:

- The wind speed decreases from its previous value (i.e., 13 m/s) to 7 m/s which turn reduces the wind power generation from 23 kW to 4.587 kW as shown in Fig. 8(b) and
- The DC load also reduces from 19.2 kW to 9.6 kWW as shown in Fig. 8(d).

The generation and load profiles of remaining components remain similar to that of the previous operating interval (i.e., from $t = 3$ s to $t = 5$ s) and this current operating scenario continues until $t = 7$ s. During this condition, the total from solar and wind on the DC-side is 15.128 kW while having the load demand as 9.6 kW. At the same time, the AC-side will have a shortage of 5.4 kW which will be exported from the DC-side as the synchronous generator is still generating 15 kW while the load demand on the AC-side is 20.4 kW. Hence, the battery will store only energy equivalent to the power of 0.178 kW which is depicted in Fig. 8(f). During these transients, the DC-link voltage is severely disturbed as compared to all other conditions. However, the designed NRBCs stabilize this in an effective way as compared to the ESMC.

Finally the AC load is reduced to 15.42 kW at $t = 7$ s from its previous value (i.e., 20.4 kW) while all reaming components are operating with similar power profiles to that of the previous step and this operation is observed until $t = 8$ s. In this condition, the bidirectional VSC will only ensure the power transfer of 0.42 kW from the DC-side to AC-side and the BESS will store more energy as compared to the previous step. Since the severity of this transient is not so significant, it does not significantly affect the power profiles of different elements as demonstrated in Fig. 8. However, the DC-link voltage is slightly affected as shown in Fig. 9 though its severity is much less than all previous conditions.

Simulation results under different transient events clearly indicate the ability of the designed NRBC in terms of enhancing the dynamic stability of the hybrid AC/DC microgrid through balancing power. Hence, the designed controller is robust against any disturbances. It is well-known that the total energy losses in common converters can be divided into two general categories: conductive losses and switching losses where switching losses are more dominant. In this work, IGBT switches are used which exhibit very low power losses. This can also be evidenced from power responses of different components over a range of scenarios. It can be seen that there are negligible power losses. Another reason for low power losses is the use of low switching frequency, i.e., 5 kHz as stated earlier in this section. Simulations results clearly demonstrate that the controller is robust against changes in solar power generation, wind power generation, and measurement disturbances.

6. Conclusion

A robust backstepping control strategy is employed to ensure the dynamic stability of hybrid AC/DC microgrid. The robust strategy is applied to obtain the control inputs for different components where all these control inputs guarantee the desired tracking of all physical states by formulating internal and virtual stabilizing functions. The dynamic stability is theoretically assessed through control Lyapunov functions by observing the decreases in the rate of changing the energy associated with different states. The external disturbances are modeled in terms of parametric uncertainties, modeling inaccuracies, and external disturbances for which control signal are determined by imposing proper bounds which in turn ensure the dynamic stability under any circumstance. Simulation results under almost all possible operating scenarios further justify the theoretical findings by improving the dynamic stability with the designed controllers for all elements in hybrid AC/DC microgrid. Though the designed controllers are used for a specific hybrid AC/DC microgrid structure, it can be employed on any microgrid which includes such components. Furthermore, the designed control scheme can be applied on any source (such as fuel cell, diesel generators, etc.) whose models can be represented through the set of differential equations. When compared to an existing controller, the newly designed controller outperforms the existing controller in every scenario. Based on the analysis presented in this paper the key achievements of this work can be summarized through following points:

- The simulation results show that the designed robust controller effectively stabilizes the DC-bus voltage under various operating conditions of the hybrid AC/DC microgrid.

- The designed robust controller enhances power-sharing both on the DC-side and AC-side with faster transients and less overshoots even with substantial fluctuations in loads and power generation from renewable nergy sources (i.e., solar and wind) which is not achievable with the existing controller.

The proposed scheme does not consider parametric uncertainties and therefore, the robustness against parametric uncertainties has not been tested. This is also a limitation of the proposed scheme, however, the future works will engage with the improvement in the proposed scheme by incorporating parametric uncertainties.

Declaration of Competing Interest

The authors declare that they have no known competing financial interests or personal relationships that could have appeared to influence the work reported in this paper.

Data availability

Data will be made available on request.

Acknowledgment

The authors would like to thank Deakin University in Australia as a part of this work was carried out during their tenure at Deakin.

References

Alam, F., Ashfaq, M., Zaidi, S.S., Memon, A.Y., 2016. Robust droop control design for a hybrid AC/DC microgrid. In: 2016 UKACC 11th International Conference on Control (CONTROL), pp. 1–6.

Baghaee, H.R., Mirsalim, M., Gharehpetian, G.B., Talebi, H.A., 2018. A decentralized power management and sliding mode control strategy for hybrid AC/DC microgrids including renewable energy resources. IEEE Trans. Ind. Inf.. 1–1

Bevrani, H., Shokoohi, S., 2013. An intelligent droop control for simultaneous voltage and frequency regulation in islanded microgrids. IEEE Trans. Smart Grid 4 (3), 1505–1513.

Chettibi, N., Mellit, A., Sulligoi, G., Massi Pavan, A., 2018. Adaptive neural network-based control of a hybrid AC/DC microgrid. IEEE Trans. Smart Grid 9 (3), 1667–1679.

Chinchilla, M., Arnaltes, S., Burgos, J.C., 2006. Control of permanent-magnet generators applied to variable-speed wind-energy systems connected to the grid. IEEE Trans. Energy Convers. 21 (1), 130–135.

Gomez-Aleixandre, C., Navarro-Rodriguez, A., Villa, G., Blanco, C., Garcia, P., 2022. Adaptive droop controller for a hybrid 375 Vdc/48 Vdc/400 Vac AC/DC microgrid. IEEE Trans. Ind. Appl. 58 (4), 5104–5116.

Hirsch, A., Parag, Y., Guerrero, J., 2018. Microgrids: a review of technologies, key drivers, and outstanding issues. Renew. Sustain. Energy Rev. 90, 402–411.

Katayama, M., Ohno, T., Obara, H., Kawamura, A., 2019. Application of multi-level converter for fast current control in small-scale DC power network. IEEE Trans. Ind. Appl.. 1–1

Liu, X., Wang, P., Loh, P.C., 2011. A hybrid AC/DC microgrid and its coordination control. IEEE Trans. Smart Grid 2 (2), 278–286.

Loh, P.C., Li, D., Chai, Y.K., Blaabjerg, F., 2013. Autonomous operation of hybrid microgrid with AC and DC subgrids. IEEE Trans. Power Electron. 28 (5), 2214–2223.

Loh, P.C., Li, D., Chai, Y.K., Blaabjerg, F., 2013. Hybrid AC-DC microgrids with energy storages and progressive energy flow tuning. IEEE Trans. Power Electron. 28 (4), 1533–1543.

Ma, T., Cintuglu, M.H., Mohammed, O., 2015. Control of hybrid AC/DC microgrid involving energy storage, renewable energy and pulsed loads. In: 2015 IEEE Industry Applications Society Annual Meeting, pp. 1–8.

Mahmud, M.A., Hossain, M.J., Pota, H.R., Oo, A.M.T., 2014. Robust nonlinear distributed controller design for active and reactive power sharing in islanded microgrids. IEEE Trans. Energy Convers. 29 (4), 893–903.

Mahmud, M.A., Hossain, M.J., Pota, H.R., Zhang, C., 2014. Investigation of critical factors affecting dynamic stability of wind generation systems with permanent magnet synchronous generators. IFAC Proc. Vol. 47 (3), 7665–7670.

Mahmud, M.A., Pota, H.R., Aldeen, M., Hossain, M.J., 2014. Partial feedback linearizing excitation controller for multimachine power systems to improve transient stability. IEEE Trans. Power Syst. 29 (2), 561–571.

Mahmud, M.A., Roy, T.K., Islam, S.N., Saha, S., Haque, M.E., 2017. Nonlinear decentralized feedback linearizing controller design for islanded DC microgrids. Electr. Power Compon. Syst. 45 (16), 1747–1761.

Mahmud, M.A., Roy, T.K., Saha, S., Haque, M.E., Pota, H.R., 2017. Control of islanded DC microgrids using nonlinear adaptive decentralized controllers. In: 2017 IEEE Industry Applications Society Annual Meeting, pp. 1–6.

Melath, G., Hussain, M.N., Agarwal, V., 2022. A nonlinear adaptive backstepping controller for stabilizing the DC bus voltage of an islanded hybrid microgrid. IEEE J. Emerg. Sel. Top.Ind. Electron. 3 (3), 538–548.

Nguyen, H.T., Kim, E., Kim, I., Choi, H.H., Jung, J., 2018. Model predictive control with modulated optimal vector for a three-phase inverter with an *LC* filter. IEEE Trans. Power Electron. 33 (3), 2690–2703.

Parhizi, S., Lotfi, H., Khodaei, A., Bahramirad, S., 2015. State of the art in research on microgrids: areview. IEEE Access 3, 890–925.

Pullaguram, D., Madani, R., Altun, T., Davoudi, A., 2022. Optimal power flow in AC/DC microgrids with enhanced interlinking converter modeling. IEEE J. Emerg. Sel. Top.Ind. Electron. 3 (3), 527–537.

Pérez-Ibacache, R., Silva, C., Yazdani, A., 2018. Linear state-feedback primary control for enhanced dynamic response of AC microgrids. IEEE Trans. Smart Grid. 1–1

Radwan, A.A.A., Mohamed, Y.A.I., 2012. Linear active stabilization of converter-dominated DC microgrids. IEEE Trans. Smart Grid 3 (1), 203–216.

Roy, T.K., Mahmud, M.A., 2018. Dynamic stability analysis of hybrid islanded DC microgrids using a nonlinear backstepping approach. IEEE Syst. J. 12 (4), 3120–3130.

Roy, T.K., Mahmud, M.A., Islam, S.N., Muttaqi, K.M., Haque, M.E., Oo, A.M.T., 2018. Control and power sharing in hybrid AC/DC microgrids using a nonlinear backstepping approach. In: 2018 IEEE Industry Applications Society Annual Meeting (IAS), pp. 1–8.

Roy, T.K., Mahmud, M.A., Oo, A.M.T., 2019. Robust adaptive backstepping excitation controller design for higher-order models of synchronous generators in multimachine power systems. IEEE Trans. Power Syst. 34 (1), 40–51.

Roy, T.K., Mahmud, M.A., Oo, A.M.T., Haque, M.E., Muttaqi, K.M., Mendis, N., 2016. Nonlinear adaptive backstepping controller design for controlling bidirectional power flow of BESSs in DC microgrids. In: 2016 IEEE Industry Applications Society Annual Meeting, pp. 1–8.

Roy, T.K., Mahmud, M.A., Oo, A.M.T., Haque, M.E., Muttaqi, K.M., Mendis, N., 2018. Nonlinear adaptive backstepping controller design for islanded DC microgrids. IEEE Trans. Ind. Appl. 54 (3), 2857–2873.

Roy, T.K., Mahmud, M.A., Shen, W., Oo, A.M.T., 2016. Non-linear adaptive coordinated controller design for multimachine power systems to improve transient stability. IET Gener. Transm. Distrib. 10 (13), 3353–3363.

Rute-Luengo, E., Navas-Fonseca, A., Gomez, J.S., Espina, E., Burgos-Mellado, C., Saez, D., Sumner, M., Muñoz-Carpintero, D., 2022. Distributed model-based predictive secondary control for hybrid AC/DC microgrids. IEEE J. Emerg. Sel. Top. Power Electron.. 1–1

Seyedi, Y., Karimi, H., Mahseredjian, J., 2022. A data-driven method for prediction of post-fault voltage stability in hybrid AC/DC microgrids. IEEE Trans. Power Syst. 37 (5), 3758–3768.

Sinha, S., Ghosh, S., Bajpai, P., 2021. Power sharing through interlinking converters in adaptive droop controlled multiple microgrid system. Int. J. Electr. Power Energy Syst. 128, 106649.

Sowmmiya, U., Govindarajan, U., 2018. Control and power transfer operation of WRIG-based WECS in a hybrid AC/DC microgrid. IET Renew. Power Gener. 12 (3), 359–373.

Sun, Q., Zhou, J., Guerrero, J.M., Zhang, H., 2015. Hybrid three-phase/single-phase microgrid architecture with power management capabilities. IEEE Trans. Power Electron. 30 (10), 5964–5977.

Wang, C., Li, X., Guo, L., Li, Y.W., 2014. A nonlinear-disturbance-observer-based DC-bus voltage control for a hybrid AC/DC microgrid. IEEE Trans. Power Electron. 29 (11), 6162–6177.

Wang, J., Jin, C., Wang, P., 2018. A uniform control strategy for the interlinking converter in hierarchical controlled hybrid AC/DC microgrids. IEEE Trans. Ind. Electron. 65 (8), 6188–6197.

Xia, Y., Peng, Y., Yang, P., Yu, M., Wei, W., 2017. Distributed coordination control for multiple bidirectional power converters in a hybrid AC/DC microgrid. IEEE Trans. Power Electron. 32 (6), 4949–4959.